Catalysis Today 453 (2025) 115258

Contents lists available at ScienceDirect

Catalysis Today

journal homepage: www.elsevier.com/locate/cattod

Conversion of dimethyl ether to hydrocarbons catalyzed by Pd-loaded *MRE zeolites

Benjamin Niethammer [a], Foteini Zormpa [a], Gia Trung Hoang [a], Nikolaj Aljoscha Slaby [a], Thomas Anthony Zevaco [a], Stamatia Karakoulia [b], Ulrich Arnold [a,*], Jörg Sauer [a]

[a] Institute of Catalysis Research and Technology (IKFT), Karlsruhe Institute of Technology (KIT), Hermann-von-Helmholtz-Platz 1, Eggenstein-Leopoldshafen 76344, Germany

[b] Chemical Process and Energy Resources Institute, Centre for Research and Technology Hellas, Thessaloniki 57001, Greece

ARTICLE INFO

Keywords:
Dimethyl ether to hydrocarbons
*MRE zeolites
Metal-modified zeolites
Palladium
Olefins
Catalyst deactivation
Fuels

ABSTRACT

The influence of Pd loading on the conversion of dimethyl ether (DME) to hydrocarbons (DTH) was investigated for *MRE-type zeolite catalysts. Catalysts with different Pd loadings were prepared by incipient wetness impregnation and characterized in terms of morphology, composition and acidity. Co-feeding of H_2 during DME conversion increased the resistance of the Pd/*MRE catalysts to deactivation, which significantly increased their lifetimes and thus conversion capacities. The product spectra show high olefin contents, comprising light olefins and higher olefins in the C_5–C_{11} range, while contents of aromatics are low. H_2 co-feeding reduces the formation of cyclic hydrocarbons and increases the formation of n- and iso-alkanes as well as olefins. Higher Pd loadings slightly decrease olefin production but increase paraffin formation, indicating direct hydrogenation of olefins on Pd nanoparticles. The olefin-rich products offer several possibilities for further processing to fuels and chemicals.

1. Introduction

Liquid hydrocarbons, owing to their high energy density and easy transport potentials, play an important role within the global energy supply chain. The utilization of non-fossil carbon sources such as biomass for the synthesis of liquid hydrocarbon fuels [1,2] or Power-to-X processes [3,4] can lead to decreased CO_2 emissions. Among these routes, methanol (MeOH) and dimethyl ether (DME) are key components, which can be processed to a series of fuels and also chemicals. One of the most important processes for DME upgrading is the DME-to-Hydrocarbon (DTH) reaction, which is similar to the Methanol-to-Hydrocarbon (MTH) reaction and allows for the production of high-quality synthetic fuels [5–8]. Compared to MeOH, the use of DME as feedstock for fuel synthesis is advantageous as DME can be synthesized directly from syngas with a lower H_2/CO ratio [9,10] or a high CO_2 content [11,12]. Contrary to the two-step synthesis via MeOH, this process is beneficial from both, thermodynamic and economical perspectives [10,13]. In the DTH process, DME exhibits a reduced heat duty, which results in a diminished adiabatic temperature rise [14]. Moreover, DME shows enhanced selectivity and space time yield in the conversion to hydrocarbon products [14], high methylation activity [15,16], as well as increased reactivity [17,18] and conversion capacity [19,20].

For the conversion of DME and MeOH to synthetic fuels, the use of heterogeneous catalysts with high thermal and chemical stability is mandatory. Some of the most important heterogeneous catalysts that are used in industrial applications are zeolites. Zeolites display high selectivity, adjustable acidity, thermal stability and comparatively simple recycling/regeneration in many catalytic processes [21]. Regarding the MTH/DTH process, zeolites of MFI framework type have been mostly utilized, resulting in the formation of hydrocarbon products with up to eleven carbon atoms [5,6,14,22–24]. Chang et al. reported that high yields of hydrocarbons can be achieved with a ZSM-5 catalyst, reaching up to 44 % selectivity and 100 % MeOH conversion at 371 °C with a LHSV of 1 h^{-1} [22,25]. The formed products were predominantly aromatics and aliphatics with carbon atoms from C_4 to C_{10}. Lee et al. reported similar results for MeOH conversion at 375 °C and a WHSV of 1 h^{-1} [14]. In this case, the use of DME as a feedstock enabled a higher hydrocarbon selectivity of 61 %.

Focusing on the reaction mechanism, in the initial phase of DME or MeOH conversion to hydrocarbons in the presence of zeolites, acid-catalyzed equilibration takes place between DME, MeOH and water

* Corresponding author.
E-mail address: ulrich.arnold@kit.edu (U. Arnold).

https://doi.org/10.1016/j.cattod.2025.115258
Received 5 December 2024; Received in revised form 7 February 2025; Accepted 27 February 2025
Available online 1 March 2025

[26]. Firstly, light olefins are produced as primary hydrocarbon products [17]. While the conversion of the reactants is increasing, methylation reactions with the first olefin products occur resulting in the formation of a hydrocarbon pool (HCP) [27,28]. Within this HCP, hydrocarbons are produced through an autocatalytic process via a dual-cycle mechanism, comprising an olefin cycle and an aromatic cycle [8,29,30]. All olefins, except ethylene, are produced from the olefin cycle. The bridging steps between the olefin and aromatic cycles are first, the bimolecular hydrogen transfer of higher olefins to yield paraffins and polyenes, and second, the cyclization of polyenes to aromatic components [29,31,32]. Inhibiting these two bridging steps would suppress the aromatic cycle, and therefore aromatics formation.

Regarding the products, a process variant that allows for the production of acyclic, branched hydrocarbons with a higher hydrogen content is desirable, thus overcoming the disadvantages associated with the production of hydrocarbon mixtures which are rich in aromatics [33–36]. Saturated products in the C_5–C_{11} chain length range can be used directly as synthetic gasoline [37] while olefins offer a high flexibility with respect to further processing, e.g. by oligomerization [38–40] or isomerization [41]. To increase the yield of olefins, a promising option is to eliminate the production of aromatics by utilizing an appropriate zeolitic catalyst with specific shape selectivity. Conventionally implemented MFI zeolites such as ZSM-5 are characterized by three-dimensional channel systems, defined by elliptical 10-ring pore structures of tetrahedra and consisting of intersecting straight and sinusoidal channels with dimensions of 5.4×5.6 Å and 5.1×5.5 Å, respectively [42]. In this context, microporous zeolite catalysts with the *MRE framework are exceptional candidates since they are characterized by one-dimensional 10-ring pore structures with the dimensions 5.3×5.6 Å, comprising unidirectional, non-overlapping channels [43,44] and thus exhibiting promising features for product selectivity in MTH/DTH reactions [45–47].

Previously, *MRE zeolites were reported to show a high selectivity to aromatics up to 40 %, low cumulative conversion capacity up to 15.8 $g_{MeOH}\ g_{cat}^{-1}$ and fast catalyst deactivation due to coking [48–50]. However, in a recent study [51], a *MRE zeolite has led to an increased yield of olefins (90 %) with a significant share of products within the C_5–C_{11} range and increased stability, enabling a cumulative conversion capacity exceeding 100 $g_{DME}\ g_{cat}^{-1}$. However, the lifetime of this catalyst was lower than that of MFI zeolites [22,45,49,51].

According to recent studies, aromatics and coke formation can be diminished by using metal modified zeolites [52–57]. Yarulina et al. showed that the surface modification of ZSM-5 zeolite with calcium decreased coke formation and improved catalyst stability by increasing its life from 11 h to 99 h, for a WHSV of 8 h^{-1} [56]. Valecillos et al. reported that the modification of ZSM-5 with zinc can improve propylene selectivity by 10 % and at the same time increase the catalyst lifetime [57]. In both cases, it was mentioned that the slowdown of the aromatic cycle could be attributed to the less strong acid sites of the zeolitic support after metal incorporation. In addition, when hydrogen is also fed to the reactant mixture, metal nanoparticles on zeolites surface can facilitate the activation and the participation of hydrogen species in the DTH reaction, which is crucial for bifunctional hydrocracking [58–61]. In the HCP, particularly polyenes are partially hydrogenated, which prevents the formation of aromatics. Among the metals, Pd shows a promising potential due to its high hydrogenation activity [62,63]. Additionally, compared to other elements, Pd exhibits a low affinity for hydrogenolysis [64].

In this work, zeolite catalysts of the *MRE type with varying Pd loadings were synthesized, characterized and used in DME conversion towards hydrocarbons. Catalysts were prepared according to the incipient wetness impregnation method, a procedure with many benefits regarding the formation of relatively small and well-defined nanoparticles [65,66]. Comprehensive characterization using XRD, Ar-physisorption, ICP-OES, SEM-EDS, TEM, NH_3-TPD and in situ FT-IR experiments with pyridine adsorption was carried out to elucidate properties of the zeolites. Performance of the catalysts was tested under reaction conditions according to previous work [51]. The impact of catalyst optimization by adding Pd as well as process modification by feeding H_2 were investigated by evaluating DME conversion, product selectivity, cumulative conversion capacity and lifetime of the catalysts.

2. Experimental

2.1. Catalyst materials and preparation

A commercially available medium pore zeolitic material with *MRE framework type and Si/Al ratio of 75 was used as support for metal deposition. All Pd-loaded zeolites were prepared according to the incipient wetness impregnation method, a procedure widely used for the deposition of small metal nanoparticles on zeolite surfaces [67]. Prior to impregnation, the zeolite was heated overnight at 70 °C. For the impregnation, a specific amount of tetraamminepalladium (II) nitrate solution (provided by Aldrich) for 0.1 wt%, 0.3 wt% and 0.5 wt% metal loadings was diluted with a certain amount of deionized water that corresponds to the total pore volume of the zeolitic support. The aqueous solution was added dropwise to the zeolite powder, which was then ground in a mortar and dried overnight at 80 °C under vacuum. As a final step, calcination of the prepared materials at 550 °C, for 6 h was carried out. Catalysts obtained via this procedure are denoted as 0.1 Pd/*MRE, 0.3 Pd/*MRE and 0.5 Pd/*MRE. Prior to each catalytic run, catalysts were reduced under a H_2 flow of 80 ml min^{-1} at 400 °C for 5 h, to be activated by generating Pd° species.

2.2. Catalyst characterization

The structural properties of the prepared catalysts were analyzed by powder X-ray diffraction (XRD) on a PANalytical X'Pert PRO diffractometer using Cu-K_α radiation ($\lambda = 0.1541$ nm), over 2 h in a 2θ range of 5–80°.

The textural characteristics of each material were obtained by Ar physisorption measurements at − 186 °C on a Quantachrome Autosorb IQ-MP2, in the vector-dose modus with a CryoTune from 3P Instruments, in a procedure according to ISO 15901-3:2007. The use of argon as adsorbate is highly recommended in the IUPAC technical report, especially for microporous materials as zeolites due to the better and faster micropore filling even at low relative pressures and the absence of interaction between the zeolites surface functional groups with argon as it occurs in the case of N_2 due to the quadrupole moment of the adsorbate [68,69]. Prior to each measurement the samples were outgassed for 12 h at 350 °C under vacuum. The total surface area was calculated using the Brunauer-Emmett-Teller (BET) method, while the micropore area was determined via the t-plot method. The total pore volume was determined from the amount adsorbed at a relative pressure of around 0.97–0.99 and the micropore volume was calculated by the non-localized density functional theory (NLDFT) kernel.

Elemental analysis was carried out by inductively coupled plasma optical emission spectroscopy (ICP-OES) using an Agilent 725 ICP-OES spectrometer (Argon plasma, 40 MHz, 2 kW). All samples were pretreated according to the microwave digestion method for solids. A small amount of each sample powder (approximately 0.5 g) was dissolved in a mixture of aqueous solutions of HNO_3 (65 %), HCl (37 %), HF (40 %) and H_2O_2 (35 %). The mixture was then treated in an Anton Paar Multiwave 3000 microwave instrument and measured.

Particle morphology and metal distribution were determined via scanning electron microscopy (SEM) in combination with energy dispersive X-ray spectroscopy (SEM-EDS). SEM images were generated on a Zeiss Gemini SEM 500 with thermal Schottky field emitter cathodes. The variable pressure system allows for pressures up to 500 Pa which is applied in the case of non-conductive samples. For the quantitative analysis of micro areas and the distribution of the elements an energy-dispersive X-ray spectrometer X-MaxN from Oxford with a

silicon drift detector size of 80 mm^2 and a resolution of 127 eV was used.

To analyze the size of Pd nanoparticles of the bifunctional Pd/*MRE catalysts, images were taken using a fully digital Tecnai Osiris™ ChemiSTEM™ scanning transmission electron microscope (STEM) from FEI company, with 200 kV acceleration voltage of the field emission cathode. The samples were imaged using a High Angle Annular Dark-Field (HAADF) detector. EDS measurements were performed with a QUANTAX system (XFlash detector, Bruker Company).

The relative number of acidic sites present in the catalysts were determined by NH_3 temperature programmed desorption (NH_3-TPD) using am Altamira chemisorption analyzer (AMI-300). The analyzer is equipped with a Thermal Conductivity Detector (TCD, rhenium-tungsten) and three mass flow controllers (MFCs, Hastings company) ruling the relevant three inlet groups, thus allowing for a great flexibility regarding the gas mixtures: Carrier (4 lines), Treatment (4 lines) and Blend (2 lines). The chemisorption equipment was piloted via the proprietary steering software ("AMI 300") from the Altamira software package, using dedicated experiment programs (.exp) whereas the evaluation of the NH_3-TPD profiles was performed using the "AMI-Analysis" part of the software package. NH_3-TPD profiles suitable for publication have been generated from the related.txt files, using the Origin Pro 2022 software package (version 9.9.0.225). According to the procedure, the samples were first reduced under a H_2/Ar stream (20 ml min^{-1} H_2 + 20 ml min^{-1} Ar) from 40 °C to 400 °C with a 5 °C min^{-1} ramp, holding the final temperature for 180 min (conditions similar to those used in the testing reactor). Afterwards, the samples were flushed with He while the temperature was decreased to 100 °C (10 °C min^{-1} ramp). Subsequently, adsorption of ammonia was performed for 60 min with a flow of 30 ml min^{-1} 5 % NH_3/He (Air Liquide Crystal gas mixture). Then, the samples were flushed for 60 min at 100 °C with 30 ml min^{-1} pure He. TPD analysis was carried out from 100 °C to 700 °C at a heating rate of 5 °C min^{-1} with 30 ml min^{-1} pure He. The composition of the exit gas was monitored online using the internal TCD. The TCD detector was calibrated after the TPD measurement using the same 5 % NH_3/He mixture (5 pulses, volume of the loop 518 µl).

The type and strength of acid sites were determined with pyridine adsorption monitored by infrared spectroscopy (IR). According to the procedure that was followed, samples were heated at 450 °C under a high vacuum (10–6 bar) for 1 h to desorb any possible physisorbed species (activation step) before pyridine adsorption and IR analysis (activation step). Spectra were collected at 150 °C to eliminate the possibility of pyridine condensation. Initially, the reference spectrum of the activated sample was collected, while pyridine equilibrium took place for 1 h. The desorption of pyridine was stepwisely monitored by evacuating the sample for 30 min at 150, 250, 350 and 450 °C and sequentially cooling down to 150 °C after each step to record the corresponding spectrum. The calculation of the acid sites was based on the integrated Lambert-Beer law (Brønsted sites: band at ~ 1540 cm^{-1} attributed to pyridinium ions [70] and Lewis sites: band at ~ 1445 cm^{-1} attributed to coordinated pyridine [71]) employing the molar extinction coefficients of Emeis [72]. More details regarding the experimental apparatus can be found elsewhere [73].

Thermal gravimetric analysis (TGA) was carried out on a TGA 2 (Mettler Toledo). The spent catalyst samples were placed in a 70 µl ALOX crucible and heated from 25 to 1000 °C (10 °C min^{-1} ramp) in a 50 ml min^{-1} flow of synthetic air (20 % O_2 in N_2, Air Liquide). For the amount of coke on the catalyst only the mass loss in the second step was taken into account.

2.3. Catalytic tests

The catalytic tests were carried out in a self-built mini-plant consisting of three parts: the feed system, the bench-scale reactor unit and the product analysis unit. The feed system consists of three gas cylinders for N_2, H_2 (Air Liquide 6.0) and DME in N_2 (8 % DME in N_2, Basi Schöberl GmbH). The gas is dosed into the plant by mass flow controllers (MFCs) from Wagner-Bronkhorst. A variable DME concentration between 8 % and 2 % can be achieved by diluting the premade mixture with the N_2 carrier. After the MFCs the gases are transferred through a heated line (180 °C) to a cylindrical fixed-bed reactor (d_i = 12 mm) with a coaxial movable thermocouple to monitor isothermal conditions. In order to achieve a plug-flow, the reactor has a 12 cm inlet zone with a packed bed of inert silicon carbide (SiC) particles ($d_{p,SiC}$ = 100–180 µm sieve fraction). The main reaction zone consists of the catalyst particles ($d_{p,cat}$ = 224–300 µm sieve fraction) which are mixed with inert SiC in a volume-ratio $\Psi_{Inert/Cat}$ = 10 to avoid hotspots and ensure plug-flow regime. For blank measurements of the educt composition there is an optional bypass. Elevated pressures up to 10 MPa can be achieved by a manually operated back-pressure regulator (TESCOM Europe). The chemical composition of the reaction mixture was analyzed with a GC-FID-TCD system (7890B, Agilent Technologies). Permanent gases, like N_2 and H_2, and H_2O, CO/CO_2 are separated by a combination of three HayeSep Q GC-columns (Agilent CP1305) in combination with a 5 Å molsieve column (Agilent CP1306) and quantified by the TCD. The hydrocarbons in turn are separated on a Poraplot Q-HT (Agilent 19095 P-Q04) and quantified by the FID. The liquid products are collected in a two-stage cold-trap cooled to − 196 °C with liquid N_2 and the C_{5+} hydrocarbons are analyzed by a Reformulyzer™ (PAC company) with a multi-dimensional PIONA (Paraffins (P), Isoparaffins (I), Olefins (O), Naphthenes (N) and Aromatics (A)) gas chromatography method in accordance to ISO 22854:2021 [74].

After filling the reactor with 0.33 g of catalyst, the reactor was heated up to 400 °C under a N_2 flow of 50 ml min^{-1} over 6 h to remove any residual moisture. The Pd-loaded catalysts were activated in a 80 ml min^{-1} H_2 flow over 5 h at 0.1 MPa. For all experiments a constant mass flow of 0.5 g_{DME} h^{-1} was chosen, which results in a weight hourly space velocity (WHSV) of 1.5 h^{-1}. For the experiments without H_2 the premade gas mixture was diluted with N_2 to achieve a concentration x_{DME} = 5 %. The H_2/DME ratio was 4:1 for all experiments with H_2. An overview of reaction conditions is given in Table 1. Time on stream (TOS) starts when switching the educt flow to the reactor. The product gas was analyzed by the online GC every 54 min. The amount of C_1-C_4 hydrocarbons, DME and MeOH was quantified in respect to calibrated gas standards, while the concentration of higher hydrocarbons (C_{5+}) was calculated in respect to the total sum of FID area. For the calculation of conversion both the concentration of DME and MeOH at the reactor outlet were taken into account. An experiment was finished when the conversion $X_{DME+MeOH}$ dropped below 40 %. The liquid products were continuously collected in the cold trap. The composition of the liquid product is therefore not time-resolved but an average over the whole "catalyst life cycle". Before analysis on the Reformulyzer™, lighter hydrocarbons were carefully evaporated at 10 °C and the organic products were separated from the aqueous products.

Table 1
Reaction conditions for the catalytic experiments.

Catalyst	Temperature (°C)	Pressure (MPa)	WHSV (h^{-1})	Feed composition	Flow rate (ml min^{-1})
*MRE *MRE-H_2 Pd/*MRE	400	2	1.5	5 % DME, 95 % N_2, or 5 % DME, 20 % H_2, 75 % N_2 5 % DME, 20 % H_2, 75 % N_2	80

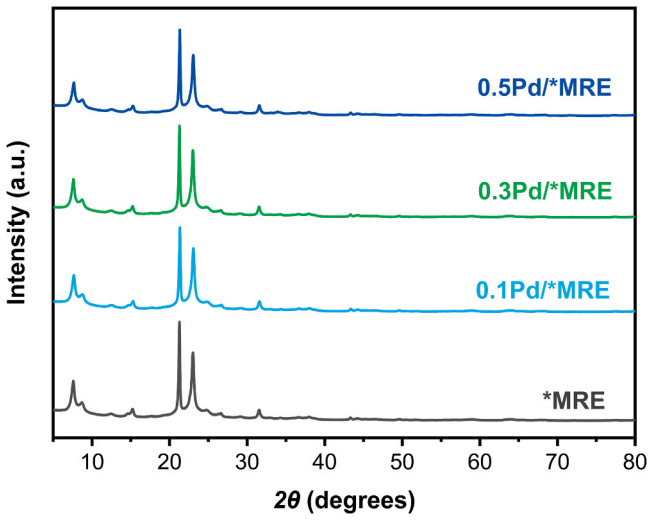

Fig. 1. XRD patterns of the *MRE zeolite and the Pd-loaded catalysts.

3. Results and discussion

3.1. Catalyst properties

The XRD patterns of the *MRE zeolite and the respective Pd-loaded catalysts are shown in Fig. 1. The typical structure of zeolites with *MRE framework was identified for all catalysts, according to the International Zeolite Association (IZA) [75], with 2θ main peaks at 7.4°, 8.6°, 21.5° and 23.2°, implying that metal introduction did not affect catalysts crystallinity. Moreover, none of the characteristic peaks for PdO or metallic Pd could be detected probably due to the low Pd content and the well distributed metal species on the surface of the zeolite.

The porosity characteristics of each catalyst are summarized in Table 2. As it can be observed, the low metal loading up to 0.5 wt% on the surface of the zeolite has no effect on the total surface area, which is maintained at around 190–200 $m^2\ g^{-1}$ for all cases. Argon adsorption-desorption isotherms are shown in Fig. S1. For low relative pressures, all catalysts exhibit Type I isotherms according to the IUPAC classification, which is characteristic for microporous materials [69]. For higher relative pressures, all isotherms change to Type II or III, probably due to the presence of empty interparticle voids, forming also a H4 type hysteresis loop, which corresponds to microporous materials with enhanced meso/macroporous characteristics. Micropore area, total pore volume and micropore volume remain also unchanged after metal loading. According to the pore size distribution (Fig. S2) determined via the NLDFT method (Argon, for zeolites with cylinder-sphere pores, adsorption branch), all catalysts contain micropores in the range of 0.5–0.6 nm, without any secondary meso/microporosity.

As it can be observed from SEM images (Fig. 2), the increase of Pd loading from 0.1 wt% up to 0.5 wt% resulted in the formation of larger nanoparticles that are well-distributed on the surface of the zeolitic support. The equal distribution of metal species was also confirmed by EDS mapping (Fig. S3), which did not show large areas with high Pd content. To verify the Pd nanoparticle size, HAADF-STEM images of the prepared catalysts were also recorded (Fig. 3). For 0.1 Pd/*MRE, no metal nanoparticles could be detected, even in low measuring distance (Fig. S4). For 0.3 wt% and 0.5 wt% metal loading, as it can be seen from the histogram (Fig. 3), small, well-defined Pd nanoparticles with a mean size of 5 nm were formed.

In Fig. 4**a**, the NH_3 desorption profiles for *MRE and the Pd-loaded *MRE zeolites are shown (temperature ramp of 5 °C min^{-1} and holding 30 min at 700 °C). The Pd-loaded materials and the parent zeolite have been initially reduced with 50 vol% H_2 in argon to draw some parallel between acidity of the catalysts and results gathered from the DTH catalytic tests.

All Pd-loaded zeolites show three characteristic, relatively similar desorption peaks, centered at 221–239 °C (low temperature peak), 391–397 °C (intermediate temperature peak) and 560–570 °C (high temperature peak), respectively. Table 3 summarizes all data gathered during NH_3-TPD. The temperatures of the desorption peaks typically indicate the different levels of acidity. Interestingly, the metal-free *MRE exhibits only the two lower peaks at 225 °C and at 382 °C, respectively, according to data from literature [76,77].

A general acidity trend regarding the Pd-loaded zeolites does not become obvious. Although the amount of acidic sites is clearly higher than that of the parent *MRE, the total amount of adsorbed NH_3

Table 2
Main characteristics of the *MRE zeolite and the Pd-loaded catalysts.

Catalyst	Pd loading (wt%)[a]	S_{BET} ($m^2\ g^{-1}$)	S_{micro} ($m^2\ g^{-1}$)[b]	V_{total} ($cm^3\ g^{-1}$)[c]	V_{micro} ($cm^3\ g^{-1}$)[d]	BAS (μmol g^{-1})[e]	LAS (μmol g^{-1})[e]	B/L ratio
*MRE	0	200	134	0.16	0.08	67	19	3.5
0.1Pd/*MRE	0.1	193	133	0.17	0.08	67	19	3.5
0.3Pd/*MRE	0.28	200	135	0.15	0.08	67	19	3.5
0.5Pd/*MRE	0.49	201	139	0.16	0.09	66	19	3.4

[a] ICP-OES measurements.
[b] t-plot method.
[c] for P/P_o 0.97.
[d] NLDFT for cumulative pore volume less than 2 nm.
[e] Pyridine FTIR.

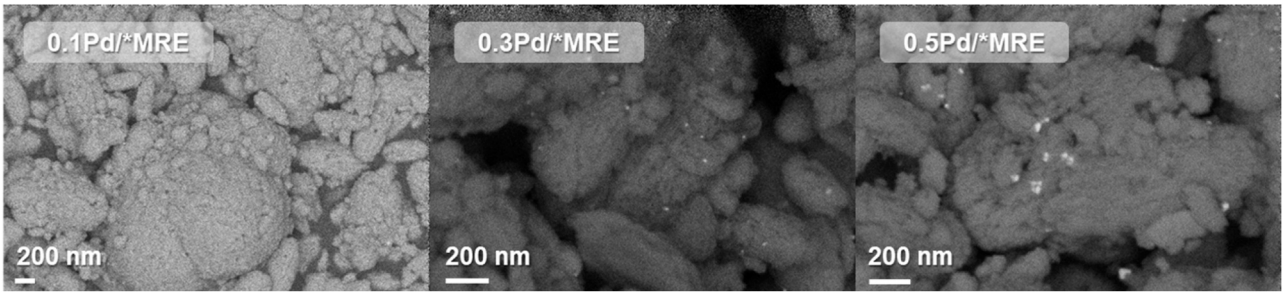

Fig. 2. SEM images of the Pd-loaded *MRE catalysts.

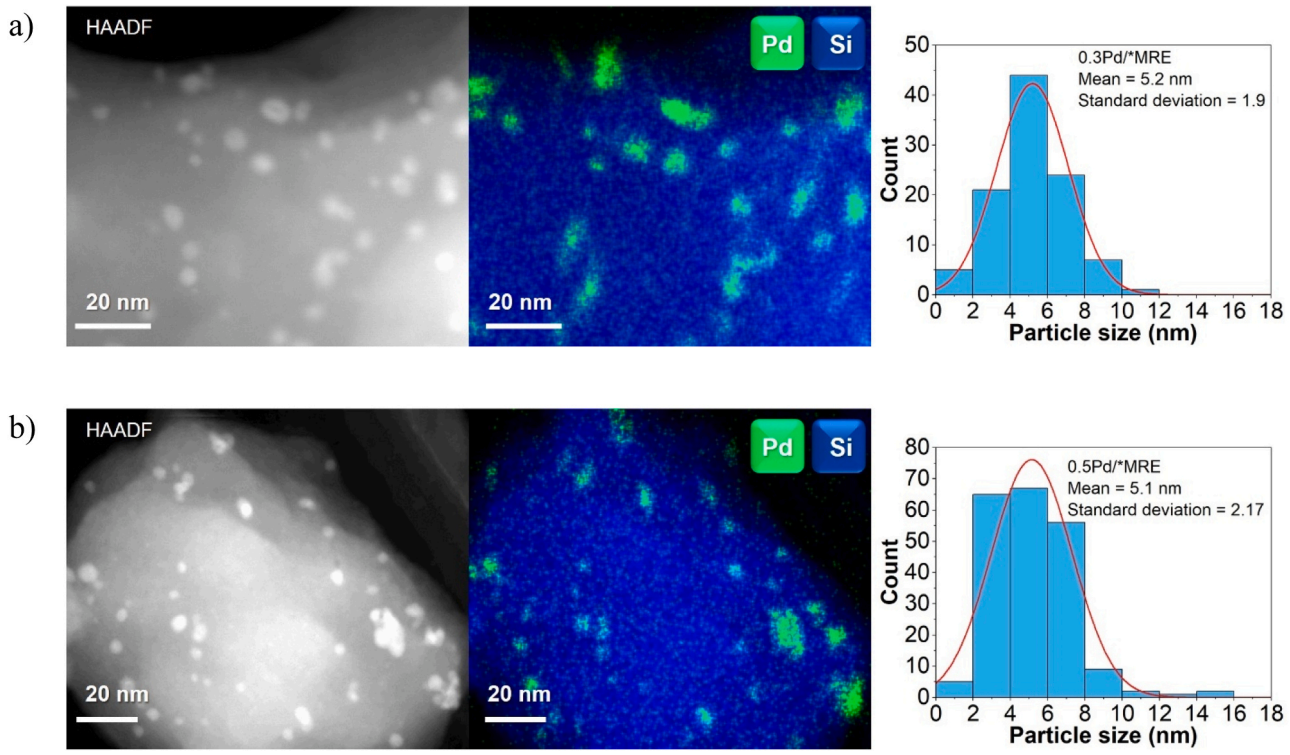

Fig. 3. HAADF-STEM images and combined mapping image of a) 0.3 Pd/*MRE and b) 0.5 Pd/*MRE catalysts. From the HAADF-STEM images the particle size distribution was calculated.

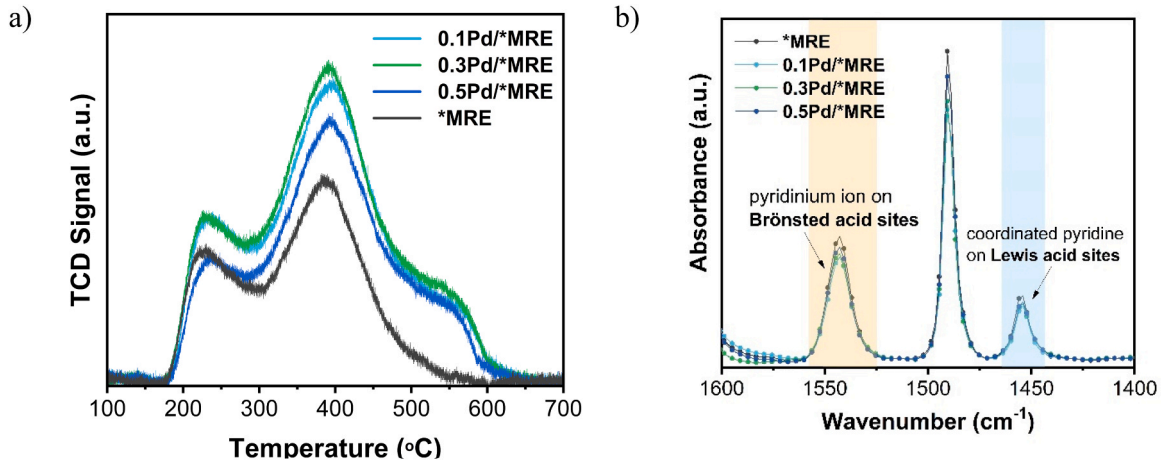

Fig. 4. a) NH_3-TPD and b) FT-IR pyridine profiles of *MRE and the Pd-loaded *MRE catalysts.

correlates not directly with the amount of metal present in the material, the 0.3 Pd/*MRE material having surprisingly the highest amount of acidic sites of the series. The low temperature peaks around 220 and 230 °C can possibly be related to the desorption of NH_3 loosely bound to the zeolite or to traces of ammonia still present in the channels of the materials and not completely removed during the 60 min purge step at 120 °C [78]. According to literature the presence of discrete acidic species like octahedrally coordinated extra framework aluminum (so-called EFAL) able to loosely bind ammonia can also explain this low temperature peak, at least partly [79,80]. Assignment of the medium and high temperature signals has to be done taking into account the relative acidities expected within the materials. The most intensive peak is located in the medium temperature range (382–397 °C) for all materials, Pd-loaded and neat zeolites, and can be tentatively attributed to ammonia strongly bound to Brønsted acidic sites [77,80]. After deconvolution of all TCD profiles into two or three Gaussian curves, this intense TCD signal represents up to 74 % of the total desorbed ammonia. By comparison, the high temperature peak around 560 °C represents only 7 up to 13 % of the total desorbed NH_3 in the case of the Pd-loaded zeolites, whereas the low temperature signal, assigned to loosely bound ammonia, represents 16–19 % in the case of the Pd-loaded *MRE and 26.5 % in the case of the neat *MRE (see Table 3). The high temperature peak, depending clearly on the presence of Pd, suggests the presence of sites which are able to bind NH_3 more strongly than in the parent *MRE zeolite. The presence of such high temperature NH_3-TPD signals was also reported by Friberg et al. for Pd supported on SZZ-13 (CHA type, small pore sized; high silica zeolite like *MRE) which was used as catalyst in methane oxidation. The SZZ-13 system is a high silica, CHA type zeolite with small pores, comparable to the *MRE zeolite, which exhibits NH_3-TPD peaks at 194, 273 and 420 °C [81]. However, the

Table 3
NH_3-TPD characteristics of *MRE and the Pd-loaded *MRE zeolites.

Catalyst	Total acid amount (μmol g^{-1})[a]	Weak acid sites		Medium acid sites		Strong acid sites	
		Peak (°C)[b]	Share (%)[c]	Peak (°C)	Share (%)	Peak (°C)	Share (%)
*MRE	144	225	26.5	382	73.5	-	-
0.1Pd/*MRE	182	239	19.3	397	74.1	570	6.6
0.3Pd/*MRE	195	221	18	391	69.2	560	12.8
0.5Pd/*MRE	184	233	16	397	72.4	563	11.6

[a] Calculated after baseline correction within the AMI-Analysis Altamira proprietary software relative to the calibration peaks.
[b] Measured using the AMI-Analysis Altamira proprietary software (see TPD profiles in Fig. S6).
[c] Relative shares calculated using Origin Pro 2024 after baseline correction and deconvolution.

exact nature of the Pd species, which cause these chemisorption phenomena, remains under debate. Pd is known for its versatile behavior once supported on zeolites. Different studies dealing with NO_x removal technologies or hydroisomerization with SZZ-13 (CHA) or ZSM-48 (*MRE) catalysts suggest that supported Pd can rearrange to form larger clusters under H_2-rich conditions and then re-disperse on the surface and partly interact with the support to build small PdO species once back under non-catalytic conditions. This behavior seems to be strongly dependent on the type and overall acidity of the zeolite supports [82,83]. Interestingly, according to the work of Zheng et al. [84] the use of low Pd-loadings (~ 0.5 wt%) with SSZ-13 plays also an important role and leads both to high dispersion and very low incorporation into the zeolite network, despite the presence of a relatively high amount of Brønsted acidic sites. This was attributed to the typical, small pore opening found in these materials (SSZ-13: ~ 3.8 Å) that greatly hinders an ion exchange between palladium species and the bulk of the zeolite. Additional data regarding NH_3-TPD measurements can be found in Fig. S5 and Fig. S6.

In order to better apprehend the cause for the high temperature NH_3-TPD peak and the possible involvement of Pd species, we performed H_2-TPR measurements with the Pd-loaded catalysts (Figs. S7 and S8). The observed pattern is typical for Pd-loaded systems: a first reduction at low temperature (positive TCD signal around − 37 °C indicating the reduction of PdO to Pd and formation of Pd hydrides) is followed by a negative signal at ~80 °C generated by the decomposition of Pd hydrides releasing H_2 [84,85]. No high temperature TPR signals ascribable to Pd species incorporated in the zeolite could be found, corroborating again the findings of the HAADF-STEM study. More information is given in the Supporting information.

Chemisorption of pyridine monitored by IR is useful to determine the number and strength of surface aprotic (Lewis) and protonic (Brønsted) acid sites on the catalyst surface [86]. Although a weaker basic molecule than ammonia and able to only titrate stronger acid sites, pyridine is able to interact via nitrogen lone-pair electrons with these acid sites giving rise to characteristic bands. The IR spectra obtained after pyridine chemisorption at 150 °C are shown in Fig. 4**b**. According to previous studies [70], the band at about 1540 cm^{-1} is attributed to the vibrational modes of Brønsted coordinated pyridine, whereas the band at 1445 cm^{-1} corresponds to vibration of pyridine chemisorbed on Lewis acid sites. An additional band which appears at 1490 cm^{-1} is also attributed to pyridine associated with both Brønsted (BAS) and Lewis acid sites (LAS) [71]. The number of BAS and LAS, as well as the BAS/LAS ratio (B/L), is tabulated in Table 2. It can be seen that all catalysts show similar amounts of Brønsted and Lewis acid sites, with B/L ratios from 3.4 to 3.5, in opposition to the NH_3-TPD results, which show an increase in the number of total acidity after Pd deposition on the surface of the zeolite. Having under consideration that pyridine is a weaker base than ammonia and thus, does not allow for the titration of very weak acid sites, we can assume that the increase of total acidity observed in the case of NH_3-TPD experiments, is mostly attributed to the additional weak acid sites of Lewis type generated after Pd modification (as identified by NH_3-TPD experiments in the temperature range from 180 to 300 °C). Considering that we are working with very low metal loadings and that *MRE is a specific small pore sized, high silica zeolite with a definite channel geometry, it seems that the temperature programmed IR chemisorption of pyridine reaches the limits with this type of materials. Additionally, pyridine being a larger molecule than ammonia, its adsorption capability differs markedly from that of ammonia, leaving aside some shares of acidic sites not easily accessible. Further information about the acidity characterization according to pyridine FT-IR measurement is given in Table S1 and Fig. S9.

3.2. Catalyst activity and deactivation behavior

The conversion of DME/MeOH over TOS for the four different catalyst systems is presented in Fig. 5. The curves clearly show that catalyst deactivation is much slower with increasing Pd loading. In the case of 0.5 Pd/*MRE, conversion starts to drop from 100 % after 350 h TOS compared to 60 h for the parent *MRE. Even in absence of Pd, co-feeding of H_2 to the parent *MRE prolongs the period of full DME conversion.

These findings are in accordance with results from Arora et al., which show that the use of H_2 as a co-feed during the MeOH to olefin (MTO) reaction at high pressure over HSAPO-34, HZSM-5 [87], HSSZ-13, HSSZ-39, HFER and HBEA catalysts [88] is mostly beneficial for prolonged catalyst stability. It was suggested that H_2 participates in hydrogen transfer reactions and inhibits the formation of dienes and other deactivating species like formaldehyde. DeLuca et al. investigated the energy barriers for hydrogenation of different species in MTO with DFT for different framework types showing that the hydrogenation of dienes and formaldehyde occurs with a lower barrier compared to the hydrogenation of butylene or propylene [89]. A recent DFT study by

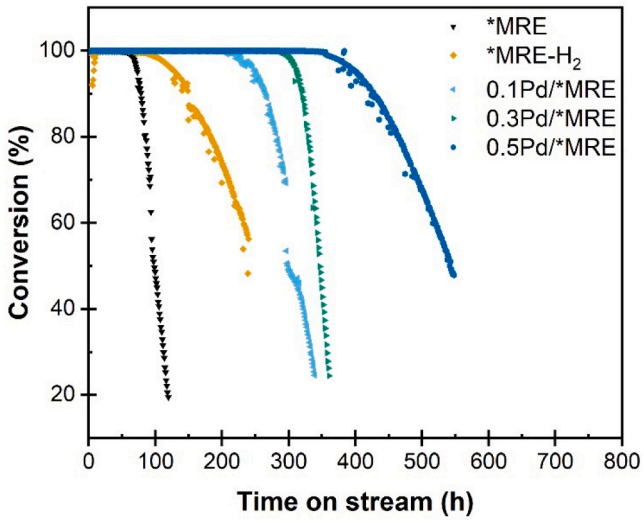

Fig. 5. DME/MeOH conversion versus TOS for the catalysts (reaction conditions: T = 400 °C, WHSV = 1.5 h^{-1}, x_{DME} = 0.05 and x_{H2} = 0.2 for the bifunctional catalysts and *MRE-H_2).

Table 4
Janssens model parameters for the catalysts ($\tau_0 = 1.536$, WHSV = 1.5 h^{-1}, $M_{DME} = 46.07$ g mol^{-1}) and the specific mass of retained coke.

Catalyst	Coefficient of deactivation (g mol^{-1})	Reaction rate coefficient (mol g_{cat}^{-1} h^{-1})	Conversion capacity ($g_{DME+MeOH}$ g_{cat}^{-1})	Specific mass of retained coke (g_{coke} g_{cat}^{-1})
*MRE	$1.52 \bullet 10^{-2}$	5.79	151.43	0.08
*MRE-H_2	$6.23 \bullet 10^{-3}$	3.68	369.54	0.06
0.1Pd/*MRE	$4.95 \bullet 10^{-3}$	8.88	465.14	0.03
0.3Pd/*MRE	$4.43 \bullet 10^{-3}$	18.08	520.19	0.06
0.5Pd/*MRE	$2.84 \bullet 10^{-3}$	6.85	809.97	0.06

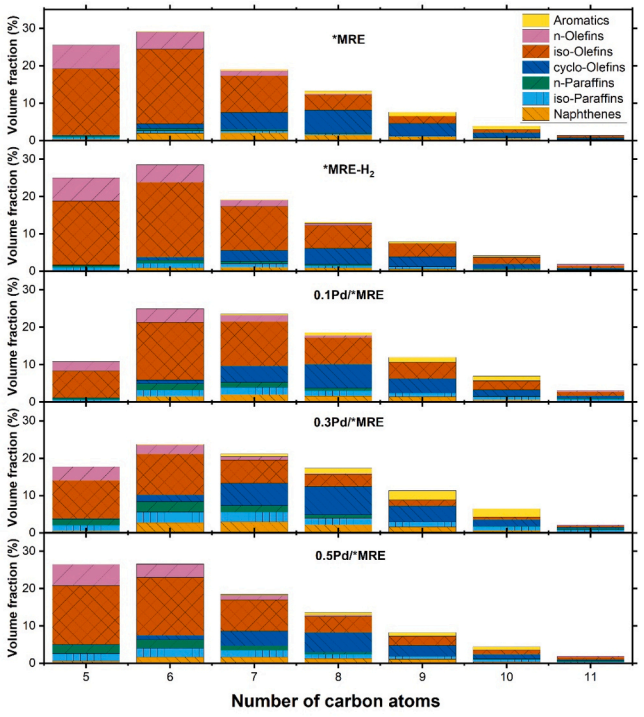

Fig. 6. Volume fractions of the liquid hydrocarbons (C_5–C_{11}) collected over the lifetime of the catalysts (until $X_{DME+MeOH}$ dropped below 40 %).

Enss et al. [90] concluded that the hydrogen transfer exhibits slightly lower barriers on the Lewis acid sites, especially for the hydrogenation of formaldehyde to MeOH. The Pd nanoparticles on the surface of the bi-functional catalysts 0.1 Pd/*MRE, 0.3 Pd/*MRE and 0.5 Pd/*MRE enable even more reaction pathways by dissociation of the H_2. By surface diffusion, these hydrogen species can participate in the reaction network, further decreasing the content of poly-unsaturated hydrocarbon species. Metal species like Pd are also known for enabling other reactions like bifunctional hydrocracking [58], hydrogenolysis [64] and hydroisomerization [77,91,92]. As the formation of hydride species is dependent on the amount of active Pd nanoparticles, it can be assumed that with an increase in Pd loading more H_2 can be integrated into the reaction network, lowering the formation of unsaturated coke precursors which in turn leads to slower deactivation.

The deactivation coefficient and conversion capacity of the catalysts were determined by fitting the Conversion-TOS curves with the Janssens model for deactivation behavior in MeOH to gasoline (MTG) reactions [93]. In this model, deactivation is described as a reduction of the effective amount of catalyst with TOS. Janssens et al. assumed that the reaction is first order in respect to MeOH and that the deactivation rate is proportional to the conversion. The activity of the catalyst is characterized by the reaction rate coefficient while deactivation behavior is described by the coefficient of deactivation. With these two parameters,

Table 5
Volume fractions of the liquid hydrocarbons (C_5–C_{11}) collected over the lifetime of the catalysts (analyses according to ISO 22854:2021).

Catalyst	Alkanes			Olefins			Aromatics
	Cyclo-	n-	Iso-	Cyclo-	n-	Iso-	
*MRE	7.7	1.8	2.7	17.1	12.8	54.8	3.1
*MRE-H_2	4.2	2.9	4.6	12.2	13.5	61.1	1.4
0.1Pd/*MRE	7.8	4.9	7.6	17.8	8.8	49.3	3.8
0.3Pd/*MRE	11.0	7.6	11.8	21.7	7.6	33.4	6.9
0.5Pd/*MRE	7.1	6.9	9.0	14.8	11.1	48.3	2.9

conversion capacities of the catalysts can be derived. For both, the H_2 co-feeding and the Pd loading, the deactivation coefficient decreases (Table 4). The deactivation coefficient decreases with increasing Pd loading but for the reaction rate coefficient, no clear correlation could be found. The overall conversion capacity increases drastically from 151.43 g_{DME} g_{cat}^{-1} for *MRE without Pd to 809.97 g_{DME} g_{cat}^{-1} for 0.5 Pd/*MRE. An overview of all fitting results is given in Table 4.

The specific amount of coke on the spent catalysts was determined by TGA according to the method described in Chapter 2.2. The *MRE catalyst shows the highest amount of coke per gram catalyst with 0.08 g_{coke} g_{cat}^{-1}. For *MRE-H_2, 0.3 Pd/*MRE and 0.5 Pd/*MRE the amount of remaining coke was slightly less with 0.06 g_{coke} g_{cat}^{-1}. Interestingly, only 0.03 g_{coke} g_{cat}^{-1} was found on the 0.1 Pd/*MRE. The results are summarized in Table 4 and the detailed TGA curves are shown in Fig. S10.

3.3. Product yields and compositions

Fig. 6 shows the volume fractions of the different liquid hydrocarbons for the individual carbon numbers (C_5–C_{11}), which have been collected over the lifetime of the catalyst. An overview of the compositions is also given in Table 5. It is obvious that C_6 hydrocarbons represent the largest share for all catalysts. As previously reported, the product spectra of *MRE show exceptionally high olefin contents, with iso- and cyclo-olefins being the predominant products [51].

In the case of the metal-free catalyst, co-feeding of hydrogen reduced the content of cyclic hydrocarbons, both saturated and unsaturated, while the formation of n- and iso-alkanes as well as olefins increased. This decrease in cyclic hydrocarbons also explains the relatively low content of aromatics found for *MRE-H_2, as cyclic hydrocarbons are the starting point of the aromatic cycle in the hydrocarbon dual-cycle concept [29,31,32]. This suggests a reduction in cyclization of polyenes coming along with enhanced formation of iso-hydrocarbons.

For the Pd-loaded catalysts, olefins are predominantly formed with volume fractions from 62 to 75.9 vol%. Similar to the parent zeolite, the olefins are mainly cyclic and iso-olefins. The distribution of products with respect to the number of carbon atoms remains largely unchanged. Only for 0.1 Pd/*MRE and 0.3 Pd/*MRE the C_5 product group is smaller than for the other catalysts. This shows that palladium is involved in product formation and influences the resulting product spectrum to a certain extent. For *MRE, 0.1 Pd*MRE and 0.5 Pd*MRE a similar

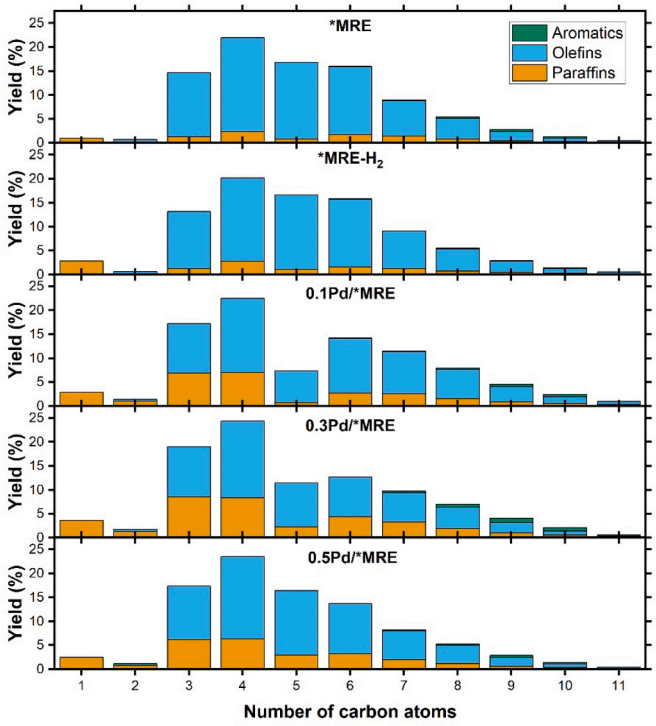

Fig. 7. Average yields of C_1–C_{11} products for *MRE and the Pd-loaded *MRE catalysts.

amount of naphthenes and cyclo-olefins was observed. With an increase in Pd loading iso- and n-olefins decrease slightly while the amount of n- and iso-paraffins increases. As mentioned above, Pd enables many reactions like hydrogenation, hydroisomerization and hydrogenolysis that are hardly possible with metal-free zeolites. The results suggest direct hydrogenation of higher olefins on the Pd nanoparticles, with the rate of hydrogenation increasing with the number of available Pd nanoparticles. The liquid product fraction of 0.3 Pd/*MRE shows a high amount of cyclic paraffins and olefins which does not correlate with the other data but could be explained by the comparatively high acidity (see Section 3.1, NH_3-TPD). Accordingly, a comparatively high content of aromatics can also be found. Detailed overviews of the liquid volume fractions for all catalysts are given in Tables S2–S6.

The average C_1–C_{11} product yields for the catalyst systems are summarized in Fig. 7. The average yields of C_5–C_{11} products were calculated by combining the C_{5+} yields from the online GC with data from the PIONA group type analyses. For all catalysts, the highest yields were observed for C_4 products ranging from 20.25 % for *MRE-H_2 to 25.53 % for 0.3 Pd/*MRE. The yields of hydrocarbon products versus DME conversion for all catalysts are shown in Fig. S11.

With the co-feeding of hydrogen, a significant increase in the yield of methane was detected for the metal-free *MRE. In the literature, different pathways for the formation of methane are described, e.g. cracking, hydrogenation of formaldehyde and hydrogenolysis [64]. Methane formation is also considered as an indicator for the deactivation by "olefine coking", in which smaller olefins adsorb on the catalyst behind the active reaction zone. These adsorbed species act as nuclei for coking when they get in contact with DME/MeOH [94,95]. For the C_2 hydrocarbons, a slight decrease in total yield was observed when co-feeding hydrogen, with a concurrent increase in ethane yield and a decrease in ethylene yield. Co-feeding of hydrogen in the case of the metal-free *MRE catalyst did not change the yields for C_3 and C_4 while the C_{5+} yield slightly decreased.

The Pd-loaded catalysts showed no significant increase in methane yields compared to experiments with the metal-free *MRE with H_2-co-feeding. In the presence of Pd, ethane yields further increased while ethylene yields remained at the same level. In previous studies, a correlation between ethylene formation and side chain methylation in the aromatic cycle has been described [29,30]. According to these studies, low ethylene formation, as observed in the case of the Pd-loaded catalysts, indicates that the aromatic cycle is suppressed in these systems. Compared to *MRE and *MRE-H_2 with hydrogen co-feed, the yields of C_3 and C_4 paraffins increased for 0.1 Pd/*MRE, 0.3 Pd/*MRE and 0.5 Pd/*MRE while the yields of olefins remained largely unchanged. As all Pd-loaded catalysts show similar total yields of C_1–C_4 products, hydrocarbon formation seems to be largely independent of the Pd loading. An overview of all hydrocarbon yields is given in Table 6.

4. Conclusions

The conversion of DME to hydrocarbons was investigated with a focus on the co-feeding of H_2 as well as the influence of varying Pd loadings on *MRE-type zeolite catalysts. The formation of small Pd nanoparticles with an average size of 2–10 nm could be ascertained for the investigated Pd loading range (0.1–0.5 wt%). From STEM EDS images it can be seen that these metallic sites are well distributed over the *MRE support. The prepared catalysts show similar characteristics as the parent *MRE regarding porosity, while the amount of overall acid sites increases.

Regarding catalytic activity, the co-feeding of H_2 clearly prolongs lifetime of the metal-free *MRE catalyst. This phenomenon is most likely due to the hydrogenation of deactivating species such as dienes and formaldehyde. Palladium greatly enhances this effect, which increases the operating time at full DME conversion from 60 h for *MRE without Pd to 350 h for 0.5 Pd/*MRE. As the Pd loading increases, the role of hydrogen gains importance in the reaction network, suppressing the build-up of coke precursors and influencing the aromatic cycle. The overall conversion capacity increases drastically from 151.43 $g_{DME}\ g_{cat}^{-1}$ for *MRE without Pd to 809.97 $g_{DME}\ g_{cat}^{-1}$ for 0.5 Pd/*MRE.

The product spectra for the liquid hydrocarbons (C_5–C_{11}) exhibit notably high olefin contents and low contents of aromatics. Co-feeding of H_2 significantly influences product compositions, reducing the shares of cyclic hydrocarbons while enhancing the formation of n- and iso-alkanes as well as olefins. Furthermore, an increase in Pd loading led to a slight decrease in the production of n- and iso-olefins, accompanied by an increase in n- and iso-paraffins. The results indicate direct hydrogenation of higher olefins, with the hydrogenation rate increasing with the availability of Pd sites.

Table 6
Percentage hydrocarbon yields for *MRE and the Pd-loaded *MRE catalysts.

	*MRE		*MRE-H_2		0.1Pd/*MRE		0.3Pd/*MRE		0.5Pd/*MRE	
	Paraffins	Olefins	Paraffins	Olefins	Paraffins	Olefins	Paraffins	Olefins	Paraffins	Olefins
C_1	0.98	-	2.86	-	2.88	-	3.69	-	2.52	-
C_2	0.03	0.70	0.17	0.47	1.00	0.44	1.33	0.46	0.84	0.36
C_3	1.32	13.41	1.3	11.88	6.93	10.33	8.55	10.52	6.21	11.16
C_4	2.36	19.61	2.81	17.44	7.04	15.46	8.32	16.04	6.36	17.17
C_{5+}[a]	51.81		52.10		49.06		47.83		48.43	

[a] Average amounts of C_{5+} hydrocarbons (paraffins + olefins + aromatics).

The obtained olefins offer several options for further processing either in chemical industry or in the fuels sector. As an example, the C_5–C_{11} fraction could be used for the production of gasoline while the light olefins could be oligomerized to higher hydrocarbons. By choice of suitable catalysts and reaction conditions this paves the way towards gasoline, kerosene and diesel fuel in a flexible and controllable manner. Provided that green methanol/DME is used for olefin production, the fuels can be obtained via sustainable pathways. This also applies to value chains within the chemical industry, where olefins play a crucial role. Regarding the catalysts, ongoing work concentrates on enhancing their performance, e.g. by varying the *MRE compositions, employing similar zeolites, substituting Pd by other metals or the preparation of shaped catalysts with tailored properties according to the envisaged applications.

CRediT authorship contribution statement

Arnold Ulrich: Writing – review & editing, Supervision, Project administration, Investigation, Funding acquisition, Conceptualization. **Niethammer Benjamin:** Writing – review & editing, Methodology, Investigation, Formal analysis. **Zormpa Foteini:** Writing – original draft, Methodology, Investigation, Formal analysis. **Hoang Gia Trung:** Writing – original draft, Methodology, Investigation, Formal analysis. **Slaby Nikolaj Aljoscha:** Writing – original draft, Methodology, Investigation, Formal analysis. **Zevaco Thomas Anthony:** Methodology, Investigation, Formal analysis, Data curation. **Karakoulia Stamatia:** Investigation, Formal analysis, Data curation. **Sauer Jörg:** Writing – review & editing, Supervision, Project administration, Conceptualization.

Declaration of Competing Interest

The authors declare that they have no known competing financial interests or personal relationships that could have appeared to influence the work reported in this paper.

Acknowledgments

The authors thank A. Lautenbach (ICP-OES), Dr. T.N. Otto (Ar-physisorption), Dr. M.C. Zimmermann (SEM micrographs) and Dr. Martin Peterlechner (TEM images) for supporting this work. Financial support from the Bundesministerium für Digitales und Verkehr (BMDV)/Fachagentur Nachwachsende Rohstoffe (FNR), Germany, within the joint research project “Renewable Fuels from Green Refineries of the Future” (FKZ: 16RK24001B) is gratefully acknowledged.

Appendix A. Supporting information

Supplementary data associated with this article can be found in the online version at doi:10.1016/j.cattod.2025.115258.

Data availability

Data will be made available on request.

References

[1] T. Verger, U. Azimov, O. Adeniyi, Biomass-based fuel blends as an alternative for the future heavy-duty transport: A review, Renew. Sustain. Energy Rev. 161 (2022) 112391, https://doi.org/10.1016/j.rser.2022.112391.
[2] M. E-Moghaddam, N. Dahmen, U. Santo, J. Sauer, Gasoline synthesis from biomass-derived syngas comparing different methanol and dimethyl ether pathways by process simulation, based on the bioliq process, Energy Fuels 38 (2024) 4229–4243, https://doi.org/10.1021/acs.energyfuels.3c04524.
[3] K. Saravanan, H. Ham, N. Tsubaki, J.W. Bae, Recent progress for direct synthesis of dimethyl ether from syngas on the heterogeneous bifunctional hybrid catalysts, Appl. Catal. B Environ. 217 (2017) 494–522, https://doi.org/10.1016/j.apcatb.2017.05.085.
[4] S. Banivaheb, S. Pitter, K.H. Delgado, M. Rubin, J. Sauer, R. Dittmeyer, Recent progress in direct DME synthesis and potential of bifunctional catalysts, Chem. Ing. Tech. 94 (2022) 240–255, https://doi.org/10.1002/cite.202100167.
[5] M. Stöcker, Methanol-to-hydrocarbons: catalytic materials and their behavior, Microporous Mesoporous Mater. 29 (1999) 3–48, https://doi.org/10.1016/S1387-1811(98)00319-9.
[6] F.J. Keil, Methanol-to-hydrocarbons: process technology, Microporous Mesoporous Mater. 29 (1999) 49–66, https://doi.org/10.1016/S1387-1811(98)00320-5.
[7] T. Mokrani, M. Scurrell, Gas conversion to liquid fuels and chemicals: the methanol route-catalysis and processes development, Catal. Rev. 51 (2009) 1–145, https://doi.org/10.1080/01614940802477524.
[8] U. Olsbye, S. Svelle, M. Bjørgen, P. Beato, T.V.W. Janssens, F. Joensen, S. Bordiga, K.P. Lillerud, Conversion of methanol to hydrocarbons: how zeolite cavity and pore size controls product selectivity, Angew. Chem. Int. Ed. 51 (2012) 5810–5831, https://doi.org/10.1002/anie.201103657.
[9] Z. Azizi, M. Rezaeimanesh, T. Tohidian, M.R. Rahimpour, Dimethyl ether: a review of technologies and production challenges, Chem. Eng. Process. Process. Intensif. 82 (2014) 150–172, https://doi.org/10.1016/j.cep.2014.06.007.
[10] Z. Wang, T. He, J. Li, J. Wu, J. Qin, G. Liu, D. Han, Z. Zi, Z. Li, J. Wu, Design and operation of a pilot plant for biomass to liquid fuels by integrating gasification, DME synthesis and DME to gasoline, Fuel 186 (2016) 587–596, https://doi.org/10.1016/j.fuel.2016.08.108.
[11] N.D. Otalvaro, G. Sogne, K.H. Delgado, S. Wild, S. Pitter, J. Sauer, Kinetics of the direct DME synthesis from CO2 rich syngas under variation of the CZA-to-γ-Al2O3 ratio of a mixed catalyst bed, RSC Adv. 11 (2021) 24556–24569, https://doi.org/10.1039/D1RA03452A.
[12] S. Polierer, D. Guse, S. Wild, K. Herrera Delgado, T.N. Otto, T.A. Zevaco, M. Kind, J. Sauer, F. Studt, S. Pitter, Enhanced direct dimethyl ether synthesis from CO2-rich syngas with Cu/ZnO/ZrO2 catalysts prepared by continuous co-precipitation, Catalysts 10 (2020) 816, https://doi.org/10.3390/catal10080816.
[13] N. Dahmen, U. Arnold, N. Djordjevic, T. Henrich, T. Kolb, H. Leibold, J. Sauer, High pressure in synthetic fuels production, J. Supercrit. Fluids 96 (2015) 124–132, https://doi.org/10.1016/j.supflu.2014.09.031.
[14] S. Lee, M. Gogate, C.J. Kulik, Methanol-to-gasoline vs. dme-to-gasolne II. Process comparison and analysis, Fuel Sci. Technol. Int. 13 (1995) 1039–1057, https://doi.org/10.1080/08843759508947721.
[15] H. Yamazaki, H. Shima, H. Imai, T. Yokoi, T. Tatsumi, J.N. Kondo, Direct production of propene from methoxy species and dimethyl ether over H-ZSM-5, J. Phys. Chem. C 116 (2012) 24091–24097, https://doi.org/10.1021/jp307290z.
[16] S. Svelle, S. Kolboe, O. Swang, U. Olsbye, Methylation of alkenes and methylbenzenes by dimethyl ether or methanol on acidic zeolites, J. Phys. Chem. B 109 (2005) 12874–12878, https://doi.org/10.1021/jp051125z.
[17] P.N. Plessow, A. Smith, S. Tischer, F. Studt, Identification of the reaction sequence of the MTO initiation mechanism using ab initio-based kinetics, J. Am. Chem. Soc. 141 (2019) 5908–5915, https://doi.org/10.1021/jacs.9b00585.
[18] P. Pérez-Uriarte, A. Ateka, A.T. Aguayo, A.G. Gayubo, J. Bilbao, Kinetic model for the reaction of DME to olefins over a HZSM-5 zeolite catalyst, Chem. Eng. J. 302 (2016) 801–810, https://doi.org/10.1016/j.cej.2016.05.096.
[19] J.S. Martinez-Espin, M. Mortén, T.V.W. Janssens, S. Svelle, P. Beato, U. Olsbye, New insights into catalyst deactivation and product distribution of zeolites in the methanol-to-hydrocarbons (MTH) reaction with methanol and dimethyl ether feeds, Catal. Sci. Technol. 7 (2017) 2700–2716, https://doi.org/10.1039/C7CY00129K.
[20] Y. Li, M. Zhang, D. Wang, F. Wei, Y. Wang, Differences in the methanol-to-olefins reaction catalyzed by SAPO-34 with dimethyl ether as reactant, J. Catal. 311 (2014) 281–287, https://doi.org/10.1016/j.jcat.2013.12.004.
[21] K. Tanabe, Industrial application of solid acid–base catalysts, Appl. Catal. Gen. 181 (1999) 399–434, https://doi.org/10.1016/S0926-860X(98)00397-4.
[22] C.D. Chang, Hydrocarbons from methanol, Catal. Rev. 25 (1983) 1–118, https://doi.org/10.1080/01614948308078874.
[23] I. Yarulina, A.D. Chowdhury, F. Meirer, B.M. Weckhuysen, J. Gascon, Recent trends and fundamental insights in the methanol-to-hydrocarbons process, Nat. Catal. 1 (2018) 398–411, https://doi.org/10.1038/s41929-018-0078-5.
[24] S. Wodarz, N.A. Slaby, M.C. Zimmermann, T.N. Otto, J. Holzinger, J. Skibsted, T. A. Zevaco, S. Pitter, J. Sauer, Shaped hierarchical H-ZSM-5 catalysts for the conversion of dimethyl ether to gasoline, Ind. Eng. Chem. Res. 59 (2020) 17689–17707, https://doi.org/10.1021/acs.iecr.9b06256.
[25] C.D. Chang, A.J. Silvestri, The conversion of methanol and other O-compounds to hydrocarbons over zeolite catalysts, J. Catal. 47 (1977) 249–259, https://doi.org/10.1016/0021-9517(77)90172-5.
[26] C. Ortega, M. Rezaei, V. Hessel, G. Kolb, Methanol to dimethyl ether conversion over a ZSM-5 catalyst: intrinsic kinetic study on an external recycle reactor, Chem. Eng. J. 347 (2018) 741–753, https://doi.org/10.1016/j.cej.2018.04.160.
[27] I.M. Dahl, S. Kolboe, On the reaction mechanism for hydrocarbon formation from methanol over SAPO-34: 2. isotopic labeling studies of the co-reaction of propene and methanol, J. Catal. 161 (1996) 304–309, https://doi.org/10.1006/jcat.1996.0188.
[28] I.M. Dahl, S. Kolboe, On the reaction mechanism for hydrocarbon formation from methanol over SAPO-34: I. Isotopic labeling studies of the co-reaction of ethene and methanol, J. Catal. 149 (1994) 458–464, https://doi.org/10.1006/jcat.1994.1312.
[29] S. Svelle, F. Joensen, J. Nerlov, U. Olsbye, K.-P. Lillerud, S. Kolboe, M. Bjørgen, Conversion of methanol into hydrocarbons over zeolite H-ZSM-5: ethene formation is mechanistically separated from the formation of higher alkenes, J. Am. Chem. Soc. 128 (2006) 14770–14771, https://doi.org/10.1021/ja065810a.

[30] M. Bjørgen, S. Svelle, F. Joensen, J. Nerlov, S. Kolboe, F. Bonino, L. Palumbo, S. Bordiga, U. Olsbye, Conversion of methanol to hydrocarbons over zeolite H-ZSM-5: on the origin of the olefinic species, J. Catal. 249 (2007) 195–207, https://doi.org/10.1016/j.jcat.2007.04.006.
[31] M. Westgård Erichsen, S. Svelle, U. Olsbye, The influence of catalyst acid strength on the methanol to hydrocarbons (MTH) reaction, Catal. Today 215 (2013) 216–223, https://doi.org/10.1016/j.cattod.2013.03.017.
[32] S. Teketel, M. Westgård Erichsen, F. Lønstad Bleken, S. Svelle, K. Petter Lillerud, U. Olsbye, Chapter 6. Shape selectivity in zeolite catalysis. the methanol to hydrocarbons (MTH) reaction, in: J. Spivey, Y.-F. Han, K. Dooley (Eds.), Catalysis, Royal Society of Chemistry, Cambridge, 2014, pp. 179–217, https://doi.org/10.1039/9781782620037-00179.
[33] Assessing the Effect of Five Gasoline Properties on Exhaust Emissions from Light-duty Vehicles Certified to Tier-2 Standards: Analysis of Data from EPAct Phase 3 (EPAct/V2/E-89), final report, U.S. Environmental Protection Agency, Washington, D.C, 2013.
[34] H. Richter, J.B. Howard, Formation of polycyclic aromatic hydrocarbons and their growth to soot—a review of chemical reaction pathways, Prog. Energy Combust. Sci. 26 (2000) 565–608, https://doi.org/10.1016/S0360-1285(00)00009-5.
[35] K. von Stackelberg, J. Buonocore, P.V. Bhave, J.A. Schwartz, Public health impacts of secondary particulate formation from aromatic hydrocarbons in gasoline, Environ. Health 12 (2013) 19, https://doi.org/10.1186/1476-069X-12-19.
[36] J. Peng, M. Hu, Z. Du, Y. Wang, J. Zheng, W. Zhang, Y. Yang, Y. Qin, R. Zheng, Y. Xiao, Y. Wu, S. Lu, Z. Wu, S. Guo, H. Mao, S. Shuai, Gasoline aromatics: a critical determinant of urban secondary organic aerosol formation, Atmos. Chem. Phys. 17 (2017) 10743–10752, https://doi.org/10.5194/acp-17-10743-2017.
[37] C. Jung, P. Seifert, F. Mehlhose, C. Hahn, D. Schröder, C. Wolfersdorf, S. Kureti, B. Meyer, Gasoline engine fuels from renewable methanol, Chem. Ing. Tech. 92 (2020) 100–115, https://doi.org/10.1002/cite.201900108.
[38] D. Takeuchi, K. Osakada, Oligomerization of olefins, in: K. Osakada (Ed.), Organomet. React. Polym., Springer Berlin Heidelberg, Berlin, Heidelberg, 2014, pp. 169–215, https://doi.org/10.1007/978-3-662-43539-7_5.
[39] C. Fuchs, U. Arnold, J. Sauer, (Co-)oligomerization of olefins to hydrocarbon fuels: influence of feed composition and pressure, Chem. Ing. Tech. 95 (2023) 651–657, https://doi.org/10.1002/cite.202200209.
[40] C. Fuchs, U. Arnold, J. Sauer, Synthesis of sustainable aviation fuels via (co–) oligomerization of light olefins, Fuel 382 (2025) 133680, https://doi.org/10.1016/j.fuel.2024.133680.
[41] X. Liu, B. Li, Q. Liu, Base-metal-catalyzed olefin isomerization reactions, Synthesis 51 (2019) 1293–1310, https://doi.org/10.1055/s-0037-1612014.
[42] D.H. Olson, W.O. Haag, R.M. Lago, Chemical and physical properties of the ZSM-5 substitutional series, J. Catal. 61 (1980) 390–396, https://doi.org/10.1016/0021-9517(80)90386-3.
[43] J.L. Schlenker, W.J. Rohrbaugh, P. Chu, E.W. Valyocsik, G.T. Kokotailo, The framework topology of ZSM-48: a high silica zeolite, Zeolites 5 (1985) 355–358, https://doi.org/10.1016/0144-2449(85)90124-1.
[44] A. Astafan, M.A. Benghalem, L. Michelin, S. Rigolet, J. Patarin, L. Pinard, T. J. Daou, Synthesis of hierarchical ZSM-48 nano-zeolites, New J. Chem. 42 (2018) 4457–4464, https://doi.org/10.1039/C7NJ04822J.
[45] J.J. Spivey, G.F. Froment, W.J.H. Dehertog, A.J. Marchi, Zeolite catalysis in the conversion of methanol into olefins, in: J.J. Spivey (Ed.), Catalysis, 1st ed., The Royal Society of Chemistry, 1992, pp. 1–64, https://doi.org/10.1039/9781847553218-00001.
[46] R.F. Lobo, H. van Koningsveld, New description of the disorder in zeolite ZSM-48, J. Am. Chem. Soc. 124 (2002) 13222–13230, https://doi.org/10.1021/ja020569v.
[47] N.C. Schjødt, P. Beato, F. Joensen, R.Y. Brogaard, L.E. Sommer, Process and plant for conversion of oxygenates, WO2023138876A1, 2023.
[48] S. Teketel, W. Skistad, S. Benard, U. Olsbye, K.P. Lillerud, P. Beato, S. Svelle, Shape selectivity in the conversion of methanol to hydrocarbons: the catalytic performance of one-dimensional 10-ring zeolites: ZSM-22, ZSM-23, ZSM-48, and EU-1, ACS Catal. 2 (2012) 26–37, https://doi.org/10.1021/cs200517u.
[49] S. Teketel, L.F. Lundegaard, W. Skistad, S.M. Chavan, U. Olsbye, K.P. Lillerud, P. Beato, S. Svelle, Morphology-induced shape selectivity in zeolite catalysis, J. Catal. 327 (2015) 22–32, https://doi.org/10.1016/j.jcat.2015.03.013.
[50] J. Zhang, Z. Huang, L. Xu, X. Zhang, X. Zhang, Y. Yuan, L. Xu, Verifying the olefin formation mechanism of the methanol-to-hydrocarbons reaction over H-ZSM-48, Catal. Sci. Technol. 9 (2019) 2132–2143, https://doi.org/10.1039/C8CY02621A.
[51] B. Niethammer, U. Arnold, J. Sauer, Suppressing the aromatic cycle of the dimethyl ether to hydrocarbons reaction on zeolites, Appl. Catal. Gen. 651 (2023) 119021, https://doi.org/10.1016/j.apcata.2023.119021.
[52] Z. Wen, C. Wang, J. Wei, J. Sun, L. Guo, Q. Ge, H. Xu, Isoparaffin-rich gasoline synthesis from DME over Ni-modified HZSM-5, Catal. Sci. Technol. 6 (2016) 8089–8097, https://doi.org/10.1039/C6CY01818A.
[53] J. Hensley, D.A. Ruddy, J.A. Schaidle, M. Behl, Catalysts and methods for converting carbonaceous materials to fuels, US20150353840A1, 2015.
[54] A. Liutkova, V. Drozhzhin, J.M.J.J. Heinrichs, V. Jestl, A. Evtushkova, B. Mezari, Á. Mayoral, N. Kosinov, E.J.M. Hensen, Role of strontium cations in ZSM-5 zeolite in the methanol-to-hydrocarbons reaction, J. Phys. Chem. Lett. 14 (2023) 6506–6512, https://doi.org/10.1021/acs.jpclett.3c01259.
[55] B. Niethammer, U. Arnold, J. Sauer, Process for converting dimethyl ether or methanol to hydrocarbons low in aromatics using a palladium-loaded zeolite catalyst, DE102021133788A1, 2023.
[56] I. Yarulina, S. Bailleul, A. Pustovarenko, J.R. Martinez, K.D. Wispelaere, J. Hajek, B.M. Weckhuysen, K. Houben, M. Baldus, V. Van Speybroeck, F. Kapteijn, J. Gascon, Suppression of the aromatic cycle in methanol-to-olefins reaction over ZSM-5 by post-synthetic modification using calcium, ChemCatChem 8 (2016) 3057–3063, https://doi.org/10.1002/cctc.201600650.
[57] J. Valecillos, E. Epelde, J. Albo, A.T. Aguayo, J. Bilbao, P. Castaño, Slowing down the deactivation of H-ZSM-5 zeolite catalyst in the methanol-to-olefin (MTO) reaction by P or Zn modifications, Catal. Today 348 (2020) 243–256, https://doi.org/10.1016/j.cattod.2019.07.059.
[58] J. Weitkamp, Catalytic hydrocracking—mechanisms and versatility of the process, ChemCatChem 4 (2012) 292–306, https://doi.org/10.1002/cctc.201100315.
[59] R. Prins, Hydrogen spillover. Facts and fiction, Chem. Rev. 112 (2012) 2714–2738, https://doi.org/10.1021/cr200346z.
[60] F. Roessner, U. Roland, Hydrogen spillover in bifunctional catalysis, J. Mol. Catal. Chem. 112 (1996) 401–412, https://doi.org/10.1016/1381-1169(96)00180-X.
[61] U. Roland, T. Braunschweig, F. Roessner, On the nature of spilt-over hydrogen, J. Mol. Catal. Chem. 127 (1997) 61–84, https://doi.org/10.1016/S1381-1169(97)00110-6.
[62] Y. Zhang, S. Zhan, K. Liu, M. Qiao, N. Liu, R. Qin, L. Xiao, P. You, W. Jing, N. Zheng, Heterogeneous hydrogenation with hydrogen spillover enabled by nitrogen vacancies on boron nitride-supported Pd nanoparticles, Angew. Chem. Int. Ed. 62 (2023) e202217191, https://doi.org/10.1002/anie.202217191.
[63] D. Sanfilippo, P.N. Rylander, Hydrogenation and dehydrogenation, in: Wiley-VCH Verlag GmbH & Co. KGaA (Ed.), Ullmanns Encycl. Ind. Chem., Wiley-VCH Verlag GmbH & Co. KGaA, Weinheim, Germany, 2009, https://doi.org/10.1002/14356007.a13_487.pub2.
[64] J.H. Sinfelt, Catalytic hydrogenolysis over supported metals, Catal. Rev. 3 (1970) 175–205, https://doi.org/10.1080/01614947008076859.
[65] B.A.T. Mehrabadi, S. Eskandari, U. Khan, R.D. White, J.R. Regalbuto, A review of preparation methods for supported metal catalysts, in: Adv. Catal., Elsevier, 2017, pp. 1–35, https://doi.org/10.1016/bs.acat.2017.10.001.
[66] Q. Zhang, S. Gao, J. Yu, Metal sites in zeolites: synthesis, characterization, and catalysis, Chem. Rev. 123 (2023) 6039–6106, https://doi.org/10.1021/acs.chemrev.2c00315.
[67] N. Wang, Q. Sun, T. Zhang, A. Mayoral, L. Li, X. Zhou, J. Xu, P. Zhang, J. Yu, Impregnating subnanometer metallic nanocatalysts into self-pillared zeolite nanosheets, J. Am. Chem. Soc. 143 (2021) 6905–6914, https://doi.org/10.1021/jacs.1c00578.
[68] M. Thommes, K. Kaneko, A.V. Neimark, J.P. Olivier, F. Rodriguez-Reinoso, J. Rouquerol, K.S.W. Sing, Physisorption of gases, with special reference to the evaluation of surface area and pore size distribution (IUPAC technical report), Pure Appl. Chem. 87 (2015) 1051–1069, https://doi.org/10.1515/pac-2014-1117.
[69] C. Schlumberger, M. Thommes, Characterization of hierarchically ordered porous materials by physisorption and mercury porosimetry—a tutorial review, Adv. Mater. Interfaces 8 (2021) 2002181, https://doi.org/10.1002/admi.202002181.
[70] R.B. Borade, A. Clearfield, Characterization of acid sites in Beta and ZSM-20 zeolites, J. Phys. Chem. 96 (1992) 6729–6737, https://doi.org/10.1021/j100195a037.
[71] R. Mokaya, W. Jones, Z. Luan, M.D. Alba, J. Klinowski, Acidity and catalytic activity of the mesoporous aluminosilicate molecular sieve MCM-41, Catal. Lett. 37 (1996) 113–120, https://doi.org/10.1007/BF00813528.
[72] C.A. Emeis, Determination of integrated molar extinction coefficients for infrared absorption bands of pyridine adsorbed on solid acid catalysts, J. Catal. 141 (1993) 347–354, https://doi.org/10.1006/jcat.1993.1145.
[73] A.C. Psarras, E.F. Iliopoulou, K. Kostaras, A.A. Lappas, C. Pouwels, Investigation of advanced laboratory deactivation techniques of FCC catalysts via FTIR acidity studies, Microporous Mesoporous Mater. 120 (2009) 141–146, https://doi.org/10.1016/j.micromeso.2008.09.014.
[74] DIN EN ISO 22854:2021-10, Liquid Petroleum Products – Determination of Hydrocarbon Types and Oxygenates in Automotive-motor Gasoline and in Ethanol (E85) Automotive Fuel – Multidimensional Gas Chromatography Method (ISO 22854:2021); German version EN ISO 22854, 2021, n.d. ⟨https://doi.org/10.31030/3262266⟩.
[75] ZSM-48: Simulated Plots, n.d. ⟨https://europe.iza-structure.org/IZA-SC/DO_structures/DO_pow_plot_diffax.php?ID=13⟩ (Accessed 30 January 2024).
[76] L. Kumar, S. Singh, S. Pai, B.L. Newalkar, M. Kumar, K.K. Pant, Investigation into ZSM-48 framework acidity for maximization of *p*-xylene in toluene methylation, Mol. Catal. 554 (2024) 113816, https://doi.org/10.1016/j.mcat.2023.113816.
[77] Y. Wang, W. Liu, W. Zhang, J. Sun, S. Li, J. Zheng, B. Fan, R. Li, Comparison of n-dodecane hydroisomerization performance over Pt supported ZSM-48 and ZSM-22, Catal. Lett. 151 (2021) 3492–3500, https://doi.org/10.1007/s10562-021-03587-8.
[78] I. Lezcano-Gonzalez, U. Deka, B. Arstad, A.V.Y.-D. Deyne, K. Hemelsoet, M. Waroquier, V.V. Speybroeck, B.M. Weckhuysen, A.M. Beale, Determining the storage, availability and reactivity of NH3 within Cu-chabazite-based ammonia selective catalytic reduction systems, Phys. Chem. Chem. Phys. 16 (2013) 1639–1650, https://doi.org/10.1039/C3CP54132K.
[79] Y. Lou, J. Ma, W. Hu, Q. Dai, L. Wang, W. Zhan, Y. Guo, X.-M. Cao, Y. Guo, P. Hu, G. Lu, Low-temperature methane combustion over Pd/H-ZSM-5: active Pd sites with specific electronic properties modulated by acidic sites of H-ZSM-5, ACS Catal. 6 (2016) 8127–8139, https://doi.org/10.1021/acscatal.6b01801.
[80] F. Lónyi, J. Valyon, On the interpretation of the NH3-TPD patterns of H-ZSM-5 and H-mordenite, Microporous Mesoporous Mater. 47 (2001) 293–301, https://doi.org/10.1016/S1387-1811(01)00389-4.
[81] I. Friberg, A.H. Clark, P.H. Ho, N. Sadokhina, G.J. Smales, J. Woo, X. Auvray, D. Ferri, M. Nachtegaal, O. Kröcher, L. Olsson, Structure and performance of zeolite supported Pd for complete methane oxidation, Catal. Today 382 (2021) 3–12, https://doi.org/10.1016/j.cattod.2020.11.026.

[82] K. Okumura, M. Niwa, Control of the dispersion of Pd through the interaction with acid sites of zeolite studied by EXAFS, Top. Catal. 18 (2002) 85–89, https://doi.org/10.1023/A:1013889129214.
[83] O. Mihai, L. Trandafilović, T. Wentworth, F.F. Torres, L. Olsson, The effect of Si/Al ratio for Pd/BEA and Pd/SSZ-13 used as passive NOx adsorbers, Top. Catal. 61 (2018) 2007–2020, https://doi.org/10.1007/s11244-018-1017-z.
[84] Y. Zheng, L. Kovarik, M.H. Engelhard, Y. Wang, Y. Wang, F. Gao, J. Szanyi, Low-temperature Pd/Zeolite passive NO $_x$ adsorbers: structure, performance, and adsorption chemistry, J. Phys. Chem. C 121 (2017) 15793–15803, https://doi.org/10.1021/acs.jpcc.7b04312.
[85] Y. Ryou, J. Lee, S.J. Cho, H. Lee, C.H. Kim, D.H. Kim, Activation of Pd/SSZ-13 catalyst by hydrothermal aging treatment in passive NO adsorption performance at low temperature for cold start application, Appl. Catal. B Environ. 212 (2017) 140–149, https://doi.org/10.1016/j.apcatb.2017.04.077.
[86] E.P. Parry, An infrared study of pyridine adsorbed on acidic solids. Characterization of surface acidity, J. Catal. 2 (1963) 371–379, https://doi.org/10.1016/0021-9517(63)90102-7.
[87] S.S. Arora, D.L.S. Nieskens, A. Malek, A. Bhan, Lifetime improvement in methanol-to-olefins catalysis over chabazite materials by high-pressure H2 co-feeds, Nat. Catal. 1 (2018) 666–672, https://doi.org/10.1038/s41929-018-0125-2.
[88] S.S. Arora, Z. Shi, A. Bhan, Mechanistic basis for effects of high-pressure H_2 cofeeds on methanol-to-hydrocarbons catalysis over zeolites, ACS Catal. 9 (2019) 6407–6414, https://doi.org/10.1021/acscatal.9b00969.
[89] M. DeLuca, C. Janes, D. Hibbitts, Contrasting arene, alkene, diene, and formaldehyde hydrogenation in H-ZSM-5, H-SSZ-13, and H-SAPO-34 frameworks during MTO, ACS Catal. 10 (2020) 4593–4607, https://doi.org/10.1021/acscatal.9b04529.
[90] A.E. Enss, P. Huber, P.N. Plessow, F. Studt, Methanol-mediated hydrogen transfer reactions at surface lewis acid sites of H-SSZ-13, J. Phys. Chem. C 128 (2024) 15367–15379, https://doi.org/10.1021/acs.jpcc.4c03408.
[91] S.J. McCarthy, G.P. Schleicher, K.M. Prentice, M. Daage, C.G. Oliveri, T.F. Degnan, J.G. Santiesteban, A.B. Dandekar, W.J. Novak, W.F. Lai, Integrated hydrocracking and dewaxing of hydrocarbons, US8394255B2, 2013.
[92] K.M. Prentice, M. Daage, A.B. Dandekar, C.G. Oliveri, R. Vijay, S.J. McCarthy, W.F. Lai, B.R. Fingland, Integrated hydrocracking and dewaxing of hydrocarbons, US9598651B2, 2017.
[93] T.V.W. Janssens, A new approach to the modeling of deactivation in the conversion of methanol on zeolite catalysts, J. Catal. 264 (2009) 130–137, https://doi.org/10.1016/j.jcat.2009.03.004.
[94] H. Schulz, M. Wei, Pools and constraints in methanol conversion to olefins and fuels on zeolite HZSM5, Top. Catal. 57 (2014) 683–692, https://doi.org/10.1007/s11244-013-0225-9.
[95] H. Schulz, “Coking” of zeolites during methanol conversion: basic reactions of the MTO-, MTP- and MTG processes, Catal. Today 154 (2010) 183–194, https://doi.org/10.1016/j.cattod.2010.05.012.